arXiv:1407.4391v1 [astro-ph.GA] 16 Jul 2014

Panchromatic Hubble Andromeda Treasury IX: A Photometric Survey of Planetary Nebulae in M31

Mark J. Veyette[1,2], Benjamin F. Williams[1], Julianne J. Dalcanton[1], Bruce Balick[1], Nelson Caldwell[3], Morgan Fouesneau[1,4], Léo Girardi[5], Karl D. Gordon[6,7], Jason Kalirai[6,8], Philip Rosenfield[9], Anil C. Seth[10]

ABSTRACT

We search Hubble Space Telescope (HST) Advanced Camera for Surveys (ACS) and Wide Field Camera 3 (WFC3) broadband imaging data from the Panchromatic Hubble Andromeda Treasury (PHAT) survey to identify detections of cataloged planetary nebulae (PNe). Of the 711 PNe currently in the literature within the PHAT footprint, we find 467 detected in the broadband. For these 467 we are able to refine their astrometric accuracy from $\sim$0.″3 to 0.″05. Using the resolution of HST, we are able to show that 152 objects currently in the catalogs are definitively not PNe, and we show that 32 objects thought to be extended in ground-based images are actually point-like and therefore good PN candidates. We also find one PN candidate that is marginally resolved. If this is a PN, it is up to 0.7 pc in diameter. With our new photometric data, we develop a method of measuring the level of excitation in individual PNe by comparing broadband and narrowband imaging and describe the effects of excitation on a PN's photometric signature. Using the photometric properties of the known PNe in the PHAT catalogs, we search for more PN, but do not find any new candidates, suggesting that ground-based emission-line surveys are complete in the PHAT footprint to $F475W \simeq 24$.

Subject headings: galaxies: individual (M31) — planetary nebulae: general

[1]Department of Astronomy, University of Washington, Box 351580, Seattle, WA 98195, USA

[2]Astronomy Department, Boston University, 725 Commonwealth Ave, Boston, MA, 02215, USA

[3]Harvard-Smithsonian Center for Astrophysics, 60 Garden Street Cambridge, MA 02138, USA

[4]Max-Planck-Institut fur Astronomie, Königstuhl 17, 69117 Heidelberg, Germany

[5]Osservatorio Astronomico di Padova – INAF, Vicolo dell'Osservatorio 5, I-35122 Padova, Italy

[6]Space Telescope Science Institute, 3700 San Martin Drive, Baltimore, MD, 21218, USA

[7]Sterrenkundig Observatorium, Universiteit Gent, Gent, Belgium

[8]Center for Astrophysical Sciences, Johns Hopkins University, Baltimore MD 21218

[9]Department of Physics and Astronomy G. Galilei, University of Padova, Vicolo dell'Osservatorio 3, I-35122 Padova, Italy

[10]Department of Physics & Astronomy, University of Utah, Salt Lake City, UT 84112

1. Introduction

As the nearest large spiral galaxy, M31 offers a unique opportunity to study planetary nebulae (PNe) on a galactic scale. Stars born with masses between 0.8-8 $M_{\odot}$ will likely go through a planetary nebula phase, making PNe good tracers of old stellar populations. Due to the short time scales between the AGB and PN phases, the distribution and kinematics of PNe are expected to be identical to their parent population. Studying PNe as a population provides insight into galactic structure and evolution. Understanding their evolution individually can provide insight into PN structure, formation, and enrichment of the interstellar medium and provide constraints for future PN evolutionary models. Studying PNe has the additional benefit of ease of detection and classification due to their strong emission features and unique spectra. Further, the population of PNe in M31 all lie at the same distance, making it possible to directly relate the luminosity and emission of a large and diverse sample of PNe.

Previous surveys have identified and studied thousands of PNe throughout the disk and bulge of M31 (Ciardullo et al. 1989; Hurley-Keller et al. 2004; Halliday et al. 2006; Merrett et al. 2006). Recent spectroscopic studies have begun to dig deeper into their physical properties (Kwitter et al. 2012; Sanders et al. 2012). The largest survey of M31 PNe to date is a deep kinematic survey performed by Merrett et al. (2006) (hereafter M06) using the purpose-built Planetary Nebula Spectrograph (Douglas et al. 2002), which can simultaneously detect PNe and measure their radial velocities. M06 identified 3300 emission-line objects in M31, of which 2615 are likely to be PNe.

Single-purpose spectroscopic surveys are very useful for studying the properties of individual PNe, but can be time consuming and costly. In contrast, multi-purpose photometric surveys can offer substantial, albeit less detailed, information about previously discovered PNe without the need for additional observations and can even be used to identify previously undiscovered PNe (Kniazev et al. 2014). Broad spectral coverage allows one to probe large spans of the spectral energy distributions of PNe and can be used in concert with spectroscopic surveys to calibrate photometric data for the study of PN emission. Although this photometric information alone is not as detailed as spectroscopic data, it is sufficient to place broad constraints on the properties of the overall strength of the PN's emission lines and underlying stellar continuum for much larger populations than are accessible spectroscopically.

PNe are typically identified by searching for objects with bright [O III] λ5007 lines. Traditional large area surveys use the difference of on- and off-band narrowband photometry to select PN candidates which are then followed up spectroscopically to exclude H II regions and Wolf-Rayet stars, which also emit strong [O III] lines. Ground based spectroscopy is limited to only the brightest PNe and restricted by atmospheric windows. For the M06 survey, spectroscopic follow up was replaced by cuts of extended objects and objects with low $F_{5007}/F_{H\alpha}$ ratios measured from narrowband imaging from the Local Group Survey (LGS) (Massey et al. 2006). While this method provided a deeper and larger survey without the need for spectroscopic follow-up, it is also subject to more contamination. High resolution imaging provides a cleaner view of the sources of the [O III]

emission, improving rejection of non-PN sources, particularly extended H II regions which are the dominant contaminating object in PN surveys.

In Section 2 of this paper we describe how we identified PNe in the PHAT catalog by cross-identification with M06. In Section 3 we present the PHAT PNe Catalog and characterize basic UV, optical, and NIR photometric properties of PNe. We discuss our results in Section 4 and summarize them in Section 5.

2. Data Acquisition and Analysis

2.1. The Panchromatic Hubble Andromeda Treasury

The Panchromatic Hubble Andromeda Treasury (PHAT) is a Hubble Space Telescope (HST) multi cycle imaging survey covering roughly 1/3 of M31's star forming disk out to 20 kpc (Dalcanton et al. 2012). Observations were made with HST using the Advanced Camera for Surveys (ACS) and Wide Field Camera 3 (WFC3) with six filters spanning the ultraviolet (WFC3/UVIS F275W and F336W), the optical (ACS/WFC F475W and F814W), and the near-infrared (WFC3/IR F110W and F160W). All data files are publicly available and described at `http://archive.stsci.edu/prepds/phat/`. For full details of the data acquisition and analysis, see Dalcanton et al. (2012).

Briefly, photometry was reduced using the DOLPHOT 1.2 (Dolphin 2000) software package which uses iterative point spread function (PSF)-fitting photometry on neighbor-subtracted images to fit the sky and PSF simultaneously. This process is done for each peak in a stack of images across different filters of the same camera. DOLPHOT aligns each image in a stack using hundreds to thousands of bright stars in the field to achieve the precise alignment needed for its photometric processing. Further internal astrometric alignment was performed for each camera. The cameras were then aligned with each other and with a global reference frame. The reference frame was provided by archival i' data from MegaCam CFHT. The error in ACS/WFC to CFHT alignment is $0\farcs05$ and the relative error in alignment across the three cameras is $0\farcs01$. Cross identification with M06 is therefore limited by the astrometric accuracy of M06 — reported to be $0\farcs34$ and $0\farcs16$ in RA and Dec respectively.

We avoided restricting our search to the PHAT point source catalogs. Rather, we cross identified PNe using the ACS "`*.phot`" files produced by DOLPHOT. We used these raw DOLPHOT output files which contain sources that may poorly fit the PSF so as not to exclude any extended PNe.

PHAT is a multi-release program that is still in progress. This paper covers only the PHAT data available at the time the work for this paper was done. PHAT consists of a total of 23 bricks, each containing 18 HST pointings. This paper covers only Bricks 2, 4, 5, 6, 8, 9, 12, 14, 15, 16, 17, 18, 19, 21, 22, and 23. Brick 1 was excluded from this paper, though currently available, due to heavy crowding effects that made it difficult to identify PNe in the inner regions of M31.

2.2. Identifying PNe in PHAT

All PNe analyzed in this paper were originally identified as part of the M06 deep kinematic survey of M31, which covered M31's disk out to a radius of 2° (27.4 kpc). M06 identified 2615 likely PNe down to a reported completeness of $m5007 \simeq 23.75$ for the [O III] λ5007 line. Of these 2615, 711 are in the current PHAT footprint. Individual PN candidates have reported uncertainties in their $m5007$ measurements of 0.07 mag and in their RA and Dec measurements of $0\farcs34$ and $0\farcs16$ respectively. We cross identified sources in the M06 catalog with photometric data from PHAT.

2.2.1. PNe in the PHAT filters

Figure 1 shows throughput curves for each of the PHAT filters overlaid on a model PN spectrum. The bandpasses of the two UV filters, F275W and F336W, overlie many weak emission lines together with a significant stellar and nebular continuum (see Bianchi et al. 1997). The majority of nebular emission line flux falls under the bandpass of the F475W filter, namely the strong emission lines: [O III] λ5007, [O III] λ4959, $H\beta$, and $H\gamma$. Therefore, F475W flux is due largely to nebular emission lines. The F814W bandpass overlies a few weak emission lines, though the majority of flux in F814W is likely due to stellar and Paschen continuum. A few weak emission lines also fall under the F110W bandpass, which could have a significant or dominant contribution to the total flux given the weaker underlying stellar continuum in the NIR. Flux in F160W, however, is most likely entirely due to continuum from the central star as there are no emission lines that could have a significant contribution to the total F160W flux. Table 1 lists likely main contributors of PNe flux in each of the PHAT filters.

The vast majority of PN emission line flux within the PHAT spectral range falls in the F475W bandpass. Thus, most PNe have unusual colors, particularly in three-color images where F475W drives the green channel. Figure 2 shows F814W:F475W:F336W R:G:B images in which PNe appear anomalously blue-green, making them easy to visually differentiate from surrounding stars. We generated equivalent images for all the PHAT data and used them to visually identify PNe, as described in the following section.

2.2.2. PHAT Astrometry and Photometry

To assess the relative positional accuracy of the M06 and PHAT catalogs, we performed an initial visual search for anomalously blue-green objects within 3 times the 1σ uncertainties of the M06 reported positions. We found likely optical counterparts as far as $2''$ from their cataloged position. We therefore adopted $3''$ (11 pc at the distance of M31) as a search radius.

There are, on average, ∼600 objects in PHAT within $3''$ of an M06 PN location. We, therefore, require additional constraints to identify the PHAT counterpart. We first take advantage of the

fact that there is a strong linear relation between the quoted M06 $m5007$ magnitude and the PHAT F475W magnitude, since the majority of F475W flux is due to the [O III] $\lambda5007$ line. We show this relation in Figure 3 for the final catalog. A linear fit to this relation finds $F475W = -0.2240 + 1.0187 \times m5007$. In addition to magnitude, we also considered cross-identifying sources based on optical color, positional offset from M06, and the "`sharpness`" and "`roundness`" of the PSF. The most distinguishing identification parameters were optical color and the expected F475W magnitude estimated from the M06 $m5007$ magnitude. The round and sharp PSF values from PHAT's photometry were used mainly to weed out artifacts and spurious objects such as cosmic rays from the uncut "`*.phot`" files.

To automatically select candidates on the basis of the above parameters, we used an initial training set of visually identified PNe. We calculated the average value and 1σ spread of each identification parameter (expected F475W, optical color, positional offset from M06, sharpness, and roundness). For each object in PHAT within $3''$ of an M06 PN location, the differences between the training set's and the object's parameter values were normalized by the 1σ spreads of the parameter values and then averaged over all parameters giving double the weight to the optical color and estimated F475W magnitude. The resulting value, noted as z_{PN}, is the object's standard score of the deviation from typical PNe identified in PHAT. Objects with $z_{PN} < 1$ are highly probable PN candidates. Objects with $z_{PN} < 1.5$ are probable PN candidates. Objects with $z_{PN} < 3$ are possible PN candidates. Eqs. 1 and 2 define z_{PN} where, for parameter x, x_{obj} is the object's value, $\bar{x}_{PN}$ is the training set's average value, and $\sigma_{x_{PN}}$ is the 1σ spread.

$$z_x \equiv \frac{|x_{obj} - \bar{x}_{PN}|}{\sigma_{x_{PN}}} \tag{1}$$

$$\begin{aligned} z_{PN} \equiv & (2z_{F475W} + 2z_{color} + z_{RA} \\ & + z_{Dec} + z_{sharp} + z_{round})/8 \end{aligned} \tag{2}$$

We attempted to identify new PNe in M31 using the optical color and F475W magnitude space occupied by the M06 PNe. We looked for [O III] emission in the LGS [O III] images (Massey et al. 2006) to confirm these candidate PNe. None of these candidates had measurable [O III] emission. Therefore, this attempt did not result in the identification of any new PNe, suggesting M06 is complete to the LGS [O III] detection limit. An earlier attempt to photometrically identify new PNe in PHAT was made by selecting sources in the bulge of M31 with $F475W < 24.0$, $F475W - F814W < -0.3$, and no matching source in the literature. Spectroscopic follow-up of 16 of these candidates found that 7 showed emission lines indicative of PNe. A larger campaign could lead to the discovery of PNe in the inner regions of M31, where previous surveys suffered extreme crowding.

Finally, all catalogs and figures presented contain only photometric measurements with a signal-to-noise ratio (SNR) greater than 4. This SNR cut, which is necessary to ensure only accurate, high-quality measurements are analyzed, resulted in the culling of 120 F275W measurements, 2 F336W measurements, 1 F814W measurement, and 29 F160W measurements.

2.2.3. Visual Assessment

To aid in the assessment of our automatic selection method, a visual catalog was created containing a PHAT 3-color image, PHAT optical CMD, LGS [O III] image, and LGS V-band image (Massey et al. 2006), for each M06 PN location that PHAT overlaps. The three objects with the lowest z_{PN} were marked in the PHAT image and CMD. A final PNe catalog was created using the one probable candidate in fields where there was only one probable candidate, and the bluest of the candidates with the three lowest z_{PN} in the cases where there were multiple probable candidates or no probable candidates. This final catalog of 467 PNe is presented in Section 3.

The visual catalog also allowed for the quick identification of possible misidentifications in the M06 catalog. Locations where there was no probable PN candidate in PHAT and resolved nebulosity in either the PHAT image or in the LGS [O III] image were marked as probable H II regions. Locations where there was no probable PN candidate in PHAT, no obvious nebulosity, clear V-band detection, and a single bright main sequence star present in the CMD with F475W much brighter than expected from $m5007$ were marked as possible stellar emission line sources, many of which may be Wolf-Rayet stars. Both H II regions and WR stars can have strong [O III] λ5007 lines, and could have been detected by M06 as [O III] emission objects. The left two panels of Figure 4 show PHAT images of likely M06 misidentifications - one marked as an H II region, the other as a stellar source. A catalog of these possible misidentifications is presented in Section 3. Of the 711 PNe in the M06 catalog that overlap the PHAT images, 152 were likely misidentified.

There were 92 cases where there were no possible PN candidates ($z_{PN} < 3$) and no obvious source of misidentification in the PHAT or LGS images. The frequency of these cases is much higher for fainter M06 PNe. For M06 PNe with $m5007 > 25$ mag, over half were found to have no PN candidate in PHAT and no source of misidentification. The right panel of Figure 4 shows a PHAT image of an M06 PN location with no PN candidate in PHAT. These cases are left out of all catalogs and figures. Figure 5 shows histograms of $m5007$ magnitude for different PHAT classifications.

3. Results

Figure 6 shows the spatial distribution of PNe in the PHAT footprint as well as the locations of possibly misidentified M06 sources. The density of PN sources falls of radially, tracing the old stellar population. Sources tagged as extended H II regions or other non-PN stellar sources are consistently found near regions of recent and on-going star formation along the disk characterized by high UV flux. Non-PN objects were selected without prior knowledge of their location.

Table 2 provides astrometric and photometric measurements in six filters ranging from near-IR to near-UV for 467 PNe in the footprint of the current PHAT release. Of the 467 PNe in the catalog, 291 have an F275W measurement, 409 have an F336W measurement, 467 have an F475W

measurement, 466 have an F814W measurement, 185 have an F110W measurement, and 156 have an F160W measurement.

Tables 3 & 4 list M06 PNe for which we found a possible source of misidentification. These non-PN objects are listed as either extended H II regions (Table 3) or non-PN stellar sources (Table 4). Astrometry and photometry for stellar sources are included when available. Of these non-PN sources, our classifications for 38 sources agree with spectroscopic classification from Sanders et al. (2012). Most of these are H II regions.

3.1. Planetary Nebula Luminosity Function

The Planetary Nebula Luminosity Function (PNLF) has been proposed as a standard candle for distance measurements (Ciardullo et al. 1989). The PNLF is described by

$$N(M5007) \propto e^{0.307 \times M5007} \left[1 - e^{3(M5007^* - M5007)}\right], \tag{3}$$

where $M5007^*$ is the absolute magnitude bright-end cut-off. The same formula can be applied to apparent magnitude when the distances to the PNe are roughly equivalent, as is the case with M31.

The upper half of Figure 7 shows the PNLF of the PHAT PNe catalog using the M06 $m5007$. The PHAT $m5007$ PNLF matches the expected form up to ∼24th magnitude, consistent with the M06 reported completeness of 23.75. The apparent magnitude bright-end cut off of the PHAT $m5007$ PNLF is $m5007^* = 20.20 \pm 0.03$, which agrees well with the M06 value of $m5007^* = 20.2 \pm 0.1$ and the Ciardullo et al. (1989) value of $m5007^* = 20.17$.

The bottom half of Figure 7 shows the PHAT PNLF using F475W magnitudes in place of $m5007$. As one would expect given Figure 1, the PHAT F475W PNLF is similar in shape to the $m5007$ PNLF up to ∼24th magnitude. There is a slight offset in the apparent magnitude bright-end cut-off between the $m5007$ and F475W PNLF and the fainter portion of the F475W PNLF appears flatter. Assuming the F475W PNLF is of the same form as the $m5007$ PNLF, the apparent magnitude bright-end cut-off of the PHAT F475W PNLF is $F475W^* = 20.69 \pm 0.03$. Assuming a distance modulus of $(m - M)_0 = 24.47 \pm 0.07$ (corresponding to a distance of 785 ± 25 kpc) (McConnachie et al. 2005), the absolute magnitude bright-end cut off of the PHAT F475W PNLF is $F475W^* = -3.78 \pm 0.08$.

3.2. CMD Distributions of the PHAT PNe

We now describe the distribution of PNe in PHAT CMDs; in Section 4.3 we discuss the evolution of PNe through the CMDs.

3.2.1. Optical

An optical CMD of PNe compared with nearby stars (Figure 8) confirms previous expectations that most PNe exist in a very blue portion of the CMD where not many stars are expected to be found. In general, PNe are distinctly brighter and bluer than neighboring stars ($<3''$) as expected from their emission-line dominated spectrum; however, there is a population of PNe that overlap with main sequence stars in Figure 8. PNe exist in a distinct region of the optical CMD as outlined by the parallelogram in Figure 8, with hand-drawn boundaries $-1.8 < F475W - F814W < 0.2$ and $22 > F814W < 27$, containing 95% of our PNe sample.

3.2.2. UV

Over 87% of PNe in the PHAT catalog have detections in F336W and 62% have detections in both UV filters. The left side of Figure 9 shows the locations on the optical CMD of PNe with and without UV detections. UV detection is much more common among PNe that are bright in F475W, as would be expected for flux due to stellar continuum with some contribution from emission lines. UV detection is also slightly more common among bluer PNe, as the brightest PNe also tend to be the bluest.

Figure 10 shows the UV CMD of the PNe with detections in both UV filters. PNe tend to be brighter and redder in the UV than other stars within $3''$. However, these neighboring stars are dominated by MS stars and there is only a slight color difference between PNe and the population of hot MS stars, as would be expected from the assumption that UV flux of PNe comes from the very hot central star. The brightest PNe have well constrained colors, while the spread in color increases for fainter F275W magnitudes which tend to be the noisiest measurements in the PHAT filter set.

3.2.3. NIR

Over 33% of PNe in our catalog have detections in both NIR filters. Nearly all PNe with detections in the NIR also have detection in F336W, 84% of which have detections in both UV filters. Thus, any PN bright enough to be detected in the NIR is almost certainly also detected in the UV, where proportionally more of the PN's bolometric flux is emitted. The right side of Figure 9 shows the locations on the optical CMD of PNe with and without NIR detections. Similar to the UV, NIR detection is much more common among PNe that are bright in F475W. However, the optical color distribution of PNe with detections in NIR is relatively flat and distinctly different from the optical color distribution of all PNe.

Figure 11 shows the NIR CMD of the PNe with detections in both NIR filters. PNe are

distinctly bluer and brighter in the NIR than stars around them, which are primarily cool RGB and AGB stars. Their distinct color in the NIR is due to the few emission lines in F110W and the lack of emission lines in F160W.

There are two NIR-bright PNe in the PHAT catalog with $F110W - F160W > 1$ that are separate from the rest of the PNe population. It is likely that the PN in each case is coincident with an NIR-bright source.

PNe are indeed unique in their photometric signal across all of PHAT's six bands—particularly their optical and NIR color. However, their most distinguishing feature by far is a booming F475W signal best probed by F475W-F814W color. Like in F475W, emission lines in F110W add additional flux that give PNe distinct NIR colors. However, as seen in Figure 12, PNe are best secluded by their optical color. Any diagnostic that used multiple bands to identify PNe would necessarily have most of its weight on F475W, as this is where the ratio of line emission to stellar continuum is largest (see Section 4.4).

3.3. Excitation Classification

Since PNe are emission line objects, we assume the majority of F475W flux is from emission lines, allowing us to estimate line flux ratios from the difference between the F475W and $m5007$ magnitudes. As seen in Figure 1, the three strongest emission lines that fall under F475W are [O III] λ5007, [O III] λ4959, and $H\beta$. Because the [O III] λ5007 to [O III] λ4959 ratio is nearly constant for all PNe, differences in the $m5007 - F475W$ color of our PNe are largely due to differences in the [O III] to $H\beta$ ratio. This ratio is a measure of ionization in the nebula and, in general, is expected to be large when the central star is very hot.

To explore the possibility of using $F475W - m5007$ as a probe of the [O III]/$H\beta$ emission line ratio, we used data from Sanders et al. (2012), who have published spectral line ratio measurements for several PNe in M31, 69 of which are in the PHAT catalog and have both $H\beta$ and [O III] λ5007 measurements. Figure 13 shows the relation between $F475W - m5007$ and the [O III] to $H\beta$ ratio, $F_{5007}/F_{H\beta}$. The large spread of the relation is likely due to differences in the underlying stellar continuum which can significantly contribute to the total F475W flux when line emission is comparatively weak. However, a relation between the relative $F475W - m5007$ and $F_{5007}/F_{H\beta}$ exists. For low values of $F_{5007}/F_{H\beta}$ (< 11), i.e. comparatively strong $H\beta$ lines, the relation is quite strong, such that PNe with lower $F_{5007}/F_{H\beta}$ values have brighter F475W magnitudes in relation to their $m5007$ magnitudes. At higher values of $F_{5007}/F_{H\beta}$, i.e. comparatively weak $H\beta$ lines, the relation saturates as the contribution of $H\beta$ to the total flux becomes indistinguishable from the continuum and weaker emission lines. Therefore, estimates of $F_{5007}/F_{H\beta}$ can only be made for PNe with $F475W - m5007 < 0.2$. Estimates of the $F_{5007}/F_{H\beta}$ ratio can be made for 170 of the 467 PNe in the PHAT catalog using Equation 4.

$$F_{5007}/F_{H\beta} = 10^{0.7835+0.7003(F475W-m5007)} \quad (4)$$

The ratio $F_{5007}/F_{H\beta}$ has been used to calculate the Excitation classification (EC) of low EC PNe ($EC < 5$) (Dopita & Meatheringham 1990; Reid & Parker 2010). We adopt the Ex_ρ method from Reid & Parker (2010) for calculating the EC of low EC PNE as defined in Equation 5.

$$EC \equiv 0.45 \times (F_{5007}/F_{H\beta}) \tag{5}$$

EC estimates for the 170 PNe with $F475W - m5007 < 0.2$ are included in Table 2 with an uncertainty of $\sigma_{EC} = \pm 1$. All PNe with $F475W - m5007 \geq 0.2$ are assumed to have EC > 3.8. As excitation increases, the contributions of other emission lines such as He II become comparable with $H\beta$ which would cause an underestimate in the PN's EC.

4. Discussion

4.1. Extinction

M31 is known to be a dusty galaxy (e.g. Draine et al. 2014, Dalcanton et al. 2014, submitted). Therefore, we need to understand how dust may be affecting our PNe photometry. To determine the degree to which the PNe sample is attenuated by extinction, we selected a subsample of PNe from "dust-free" regions as determined from the extinction maps of Dalcanton et al. 2014 (submitted). These PNe were selected to be in regions with A_V<0.5 and a low fraction of reddened stars. Their optical CMD is shown in Figure 14, and the distribution is qualitatively equivalent to that of the full sample. Perhaps because PNe tend not to be associated with ongoing star formation or because PNe are associated with old stars (> 1 Gyr) that have migrated out of the galactic plane, our PNe photometry appears to be relatively unaffected by dust extinction.

4.2. PNLF

The consistency of the PHAT $m5007$ PNLF with the M06 PNLF suggests that the PHAT PNe catalog is a representative and unbiased subset of the M06 catalog. Despite the fact that the F475W bandpass covers emission lines other than [O III] λ5007 and continuum from the central star, the PHAT F475W PNLF is similar in form to the $m5007$ PNLF, particularly on the bright-end – aside from a slight offset. This is because the contribution by stellar continuum and weaker emission lines to the total F475W flux is less significant in brighter PNe, for which the F475W magnitude is a good indicator of $m5007$, making the F475W PNLF a possible proxy for the traditional $m5007$ PNLF for future extragalactic surveys. The flatness of the faint-end of the PHAT F475W PNLF could be due to the larger relative contribution by stellar continuum for PNe with weaker [O III] emission.

4.3. Excitation Classification and PN Evolution

Excitation classification has been found to depend on the evolutionary state of a PN, which is reflected in the central star's effective temperature, the PN's radius, and the PN's expansion velocity (Dopita et al. 1987, 1988; Dopita & Meatheringham 1990, 1991a,b; Gurzadyan & Egikian 1991; Reid & Parker 2010). Because many parameters affect the EC, the correlations between EC and physical properties of PNe have large scatter which, coupled with the large uncertainties of our own EC estimates, means we cannot reliably estimate individual parameters. However, our ability to isolate a subsample of low EC PNe allows us to place some PNe in the evolutionarily young phase with small sizes and low central star temperatures. For the remainder of this paper, we referred to PNe with EC below the upper limit of our ability to determine EC ($EC < 3.8$) as low EC PNe and all other PNe as medium to high EC PNe; note that the canonical definition of "low EC" includes up to an EC of 5. We do expect some cross contamination due to the large uncertainties in our $F475W - m5007$ measurements such that some PNe in our sample of low EC PNe are in fact medium to high EC PNe and vice versa. In addition, some high EC PNe may be misclassified as low EC PNe due to increased contribution of He II and other weak lines in the F475W bandpass.

According to PN evolutionary tracks based on photoionization models described in Dopita & Meatheringham (1990) and Reid & Parker (2010), all PNe, regardless of their initial mass, begin as low EC PNe. They then increase in EC as they evolve to a mass-dependent maximum EC before returning to a slightly lower EC. Only lower mass PNe (central star stellar mass $\lesssim 0.6 M_{\odot}$) are expected to return to an EC lower than 5. The majority of low EC PNe in our catalog are therefore likely to be young, but with a wide range of initial masses. Additionally, high EC PNe in our catalog are expected to cover the entire range of PNe ages except for the youngest.

Another set of PN evolutionary models useful for understanding how PNe evolve through PHAT color-magnitude and color-color diagrams are 1D radiation-hydrodynamic models that describe the evolution of PNe by modeling a circumstellar envelope along with the central star as it evolves from the AGB toward the white-dwarf cooling path (Perinotto et al. 2004). Studies of the emission properties of these models (e.g. Schönberner et al. 2007; Méndez et al. 2008) explain that in early stages of evolution, PNe increase in $m5007$ brightness as they increase in EC until they reach a maximum $m5007$ brightness. The intensity and duration of maximum m5007 brightness is mass-dependent. In general, higher mass progenitors result in brighter maximum m5007 but for shorter duration than fainter low mass progenitors. (Kwok 2000). Maximum $m5007$ brightness is reached at ECs higher than the upper limit of our ability to determine EC of PNe in PHAT. Therefore, we expect the PNe in our catalog to evolve from low EC to high EC simultaneously increasing in $m5007$ brightness to a maximum brightness. Indeed, this is the qualitative behavior observed in Figure 15, as described below.

4.3.1. PN Evolution Through CMDs

Figure 15 shows the locations of low EC and medium to high EC PNe on an optical CMD. We see a bifurcation of low EC and medium to high EC PNe among PNe with F475W < 23.5. This behavior would be consistent with the evolutionary transition of a high mass progenitor along, or parallel to, Side 1 (the upper boundary in the figure) as the PN's [O III] λ5007 flux reaches a maximum. The proposed transition aligns well with the PN evolutionary models described above, namely a transition from low EC to higher EC and from fainter F475W magnitudes to the brightest. Brightening in F475W along Side 1 toward the bluer portion of the CMD corresponds to evolution with a constant F814W magnitude.

The less distinct red boundary indicated by Side 2 in Figure 15 is made up of mostly low EC PNe and overlaps main sequence stars. The overlap with the main sequence is most likely due to interstellar reddening of young PNe but could also indicate residual contamination from WR stars. The faint boundary (Side 3) and the similar boundary for field stars are products of the cuts in signal-to-noise.

Figure 16 shows the locations of low EC and medium to high EC PNe on a UV CMD. The low EC PNe are systematically brighter and bluer, suggesting some transition toward redder and fainter UV magnitudes as they evolve into higher ECs. The slightly redder extant of the PN distribution compared to bright MS stars is likely due to increased contribution from nebular continuum in the F336W bandpass. Also shown in Figure 16 are two Post-AGB (P-AGB) evolutionary tracks from Vassiliadis & Wood (1993) converted to WFC3/UVIS photometry as described in Girardi et al. (2008), shown without extinction correction. We see an increased spread of UV color at fainter F275W magnitudes, but it is hard to say for certain if the spread represents the true spread in PNe UV color, or is due to photometric uncertainty and/or interstellar reddening. Still, it is clear that reduced UV flux is a prominent difference between low EC and medium to high EC PNe on the UV CMD. Such a transition is expected from P-AGB evolutionary tracks.

Figure 17 shows the CMD for F336W-F475W vs F336W. Because F336W is dominated by stellar and nebular continuum and F475W by line emission, this diagram compares emission line flux to underlying continuum. Low EC PNe appear much like hot stars, but medium to high EC PNe show up where few stars are expected to be found. The increased excitation increases flux in the emission line-dominated F475W bandpass, pulling PNe redward to a relatively unpopulated portion of the CMD. This diagnostic may be useful for future studies of PNe as it is possible to replicate through ground-based observations. Of the six PHAT filters, PNe are brightest in F336W and F475W.

In the NIR there is no separation in either color or magnitude between low EC and medium to high EC PNe. MS stars in PHAT are expected to have NIR colors redder than $F110W - F160W = 0$, with only younger MS stars (< 100 Myr) expected to have bluer colors at $F110W < \sim$23. The lack of young MS stars neighboring PNe (Figure 11) emphasizes that PNe are not sampling regions with very recent star formation.

4.4. Spectral Energy Distributions

For PNe with detections in all six PHAT filters, converting from magnitude to total flux produces Spectral Energy Distributions (SEDs) covering 0.3 to 1.6 microns. Such SEDs will provide constraints for future models of PNe evolution. Such models will be necessary to reliably constrain extinction for these PNe. Figure 18 shows SEDs for 130 PNe with detections in all six filters.

The right column of Figure 18 shows SEDs grouped by $m5007$. SEDs of the brightest PNe are largely uniform while SEDs of fainter PNe show more variations. The SEDs look much like those of hot stars with the addition of a prominent peaks at 0.475 and 1.1 microns due to emission lines in the bandpasses. However, unlike hot stars, flux at 0.336 microns exceeds flux at 0.275 microns for many PNe. This could be due to the fact that 0.275 micron flux is more attenuated by extinction, combined with the larger uncertainties in 0.275 micron flux.

The left column of Figure 18 shows SEDs grouped by EC. At the lowest EC, the SEDs show little evidence of emission line flux above the blue stellar continuum. Moving through higher EC, the emission line features become much more prominent. Again, this suggests low EC PNe are largely young PNe with the lowest EC PNe being just beyond the emergence of [O III] lines, which grow stronger as PNe evolve to higher EC.

The two anomalously NIR-bright PNe also show up in the SEDs. Again, it is likely they are crowded by a NIR-bright source.

4.5. Resolved PNe and Size Estimates

PNe are commonly found to have radii on the order of 0.1 pc but have been known to have radii as large as 0.6 pc (Phillips 2003). It might be expected that PNe with radii >0.5 pc could be resolved in PHAT considering HST's ACS camera has a plate scale of $0\farcs05$/pixel (0.2 pc/pixel at the distance of M31) and the average full width at half max (FWHM) of PHAT's PSF is ∼2 pixels. However, as PNe evolve they both expand radially and drop in luminosity, resulting in a steep decline of surface brightness. PNe large enough to be resolved in PHAT are likely too faint to be detected in PHAT. At intermediate stages of evolution, however, some PNe may be bright enough to be detected in PHAT and large enough to be slightly resolved. Figure 19 shows the dependence of FWHM on magnitude in PHAT data. Faint sources in crowded regions suffer heavy blending that can cause the direct FWHM measurement to overestimate the true FWHM. However, the FWHM distribution of PNe is indistinguishable from that of nearby stars, suggesting that PNe are not resolved in PHAT.

In general, the PNe sample does not appear any more extended than nearby stars, however, we found one PN (M06 143) that appeared significantly larger than the surrounding stars. We show an image of this PN in Figure 20. This PN has a FWHM of ∼4 pixels, compared to stars in the area, which have FWHMs of ∼2 pixels. After accounting for the effects of a $0\farcs1$ FWHM point

spread function, the intrinsic radius of the PN would be up to 0.″08, or 0.3−0.4 pc. The PHAT magnitudes of M06 143 are likely underestimated due to the extended nature of the PSF. This is supported by the fact that M06 143 is the faintest PN in our sample, with $F475W = 26.15$, and has $F475W - m5007 = 1.4$ — the largest difference of the PNe sample and more than three times the $F475W - m5007$ saturation limit of the PNe sample. Though the optical color of M06 143 is consistent with PNe in PHAT, we cannot rule out the possibility it is a blended source or a non-PN source.

Finally, any M06 source that was visually resolved in PHAT was rejected as being a PN (M06 143 is the only marginally extended PN) and classified as a possible H II region. Therefore, inclusion in Table 3 serves as an updated classification of extended objects in M06, which will be more reliable than such classifications from the ground-based data.

5. Summary

We have identified 467 PNe in the PHAT survey photometry catalogs. The F475W broadband magnitudes show a tight correlation with the $m5007$ magnitudes clearly indicating the purity of our sample. These PNe are unresolved and dominated by [O III] line emission. Since the PHAT astrometric solution is precise to 0.″01, we have provided improved astrometry for all of the PNe in our sample, along with 6-band photometry from the PHAT survey.

Comparing our broadband magnitudes and M06 narrowband magnitudes to excitation classifications from optical spectroscopy in the literature shows that low excitation PNe tend to have bluer colors in F475W-$m5007$, suggesting that our broadband magnitudes in these cases probe the emission from the central star. These results indicate that our SEDs will be useful for constraining models of PNe and central star evolution.

The size distribution of PNe in our HST images are consistent with that of point sources. However, there is some evidence that at least one PN is marginally resolved, corresponding to a physical radius of up to 0.3−0.4 pc.

Support for this work was provided by NASA through grant GO-12055 from the Space Telescope Science Institute, which is operated by the Association of Universities for Research in Astronomy, Incorporated, under NASA contract NAS5-26555.

REFERENCES

Bianchi, L., Vassiliadis, E., & Dopita, M. 1997, ApJ, 480, 290

Ciardullo, R., Jacoby, G. H., Ford, H. C., & Neill, J. D. 1989, ApJ, 339, 53

Dalcanton, J. J., Williams, B. F., Lang, D., et al. 2012, ApJS, 200, 18

Dolphin, A. E. 2000, PASP, 112, 1383

Dopita, M. A., Meatheringham, S. J., Wood, P. R., et al. 1987, ApJ, 315, L107

Dopita, M. A., Meatheringham, S. J., Webster, B. L., & Ford, H. C. 1988, ApJ, 327, 639

Dopita, M. A., & Meatheringham, S. J. 1990, ApJ, 357, 140

Dopita, M. A., & Meatheringham, S. J. 1991a, ApJ, 367, 115

Dopita, M. A., & Meatheringham, S. J. 1991b, ApJ, 377, 480

Douglas, N. G., Arnaboldi, M., Freeman, K. C., et al. 2002, PASP, 114, 1234

Draine, B. T., Aniano, G., Krause, O., et al. 2014, ApJ, 780, 172

Ferland, G. J., Porter, R. L., van Hoof, P. A. M., et al. 2013, RMxAA, 49, 137

Girardi, L., Dalcanton, J., Williams, B., et al. 2008, PASP, 120, 583

Gurzadyan, G. A., & Egikian, A. G. 1991, Ap&SS, 181, 73

Halliday, C., Carter, D., Bridges, T. J., et al 2006, MNRAS, 369, 97

Hurley-Keller, D., Morrison, H. L., Harding, P., & Jacoby, G. H. 2004, ApJ, 616, 804

Kniazev, A. Y., Grebel, E. K., Zucker, D. B., et al. 2014, AJ, 147, 16

Kwitter, K. B., Lehman, E. M. M., Balick, B., & Henry, R. B. C. 2012, ApJ, 753, 12

Kwok, S. 2000, The Origin and Evolution of Planetary Nebulae (Cambridge: Cambridge Univ. Press)

Marigo, P., Girardi, L., Groenewegen, M. A. T., & Weiss, A. 2001, A&A, 378, 958

Marigo, P., Girardi, L., Weiss, A., Groenewegen, M. A. T., & Chiosi, C. 2004, A&A, 423, 995

Massey, P., Olsen, K. A. G., Hodge, P. W., et al. 2006, AJ, 131, 2478

McConnachie, A. W., Irwin, M. J., Ferguson, A. M. N., et al. 2005, MNRAS, 356, 979

Méndez, R. H., Teodorescu, A. M., Schönberner, D., Jacob, R., & Steffen, M. 2008, ApJ, 681, 325

Merrett, H. R., Merrifield, M. R., Douglas, N. G., et al. 2006, MNRAS, 369, 120

Perinotto, M., Schönberner, D., Steffen, M., & Calonaci, C. 2004, A&A, 414, 993

Phillips, J. P. 2003, Astronomische Nachrichten, 324, 191

Reid, W. A., & Parker, Q. A. 2010, PASA, 27, 187

Sanders, N. E., Caldwell, N., McDowell, J., & Harding, P. 2012, ApJ, 758, 133

Schlafly, E. F., & Finkbeiner, D. P. 2011, ApJ, 737, 103

Schönberner, D., Jacob, R., Steffen, M., & Sandin, C. 2007, A&A, 473, 467

Thilker, D. A., Hoopes, C. G., Bianchi, L., et al 2005, ApJ, 619, L67

Vassiliadis, E., & Wood, P. R. 1993, ApJ, 413, 641

This preprint was prepared with the AAS LaTeX macros v5.2.

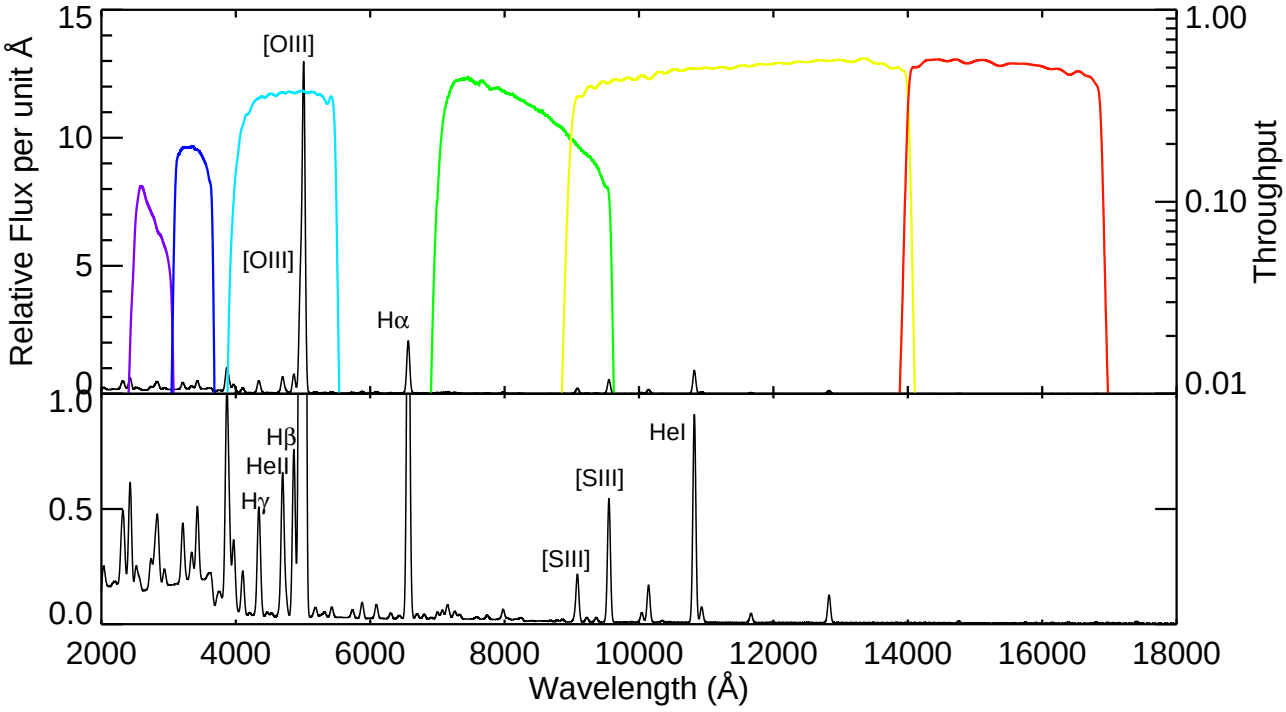

Fig. 1.— (Top) A model spectrum (black line) for a PN model close to its maximum [O III] λ5007 luminosity and with high excitation. This particular model was extracted from the Marigo et al. (2001, 2004) database of simplified evolutionary models, in which the photoionization of a spherically symmetric expanding shell is simulated with Ferland et al. (2013) Cloudy code v08.01. Some of the main contributors to the nebular flux are marked in the figure. In addition, there is a significant flux contribution from the stellar and nebular continuum, especially in the UV, as listed in Table 1. Also shown are filter throughput curves (colored lines) for filters: (from left to right) F275W, F336W, F475W, F814W, F110W, and F160W. (Bottom) A closer look at the continuum and weaker emission lines.

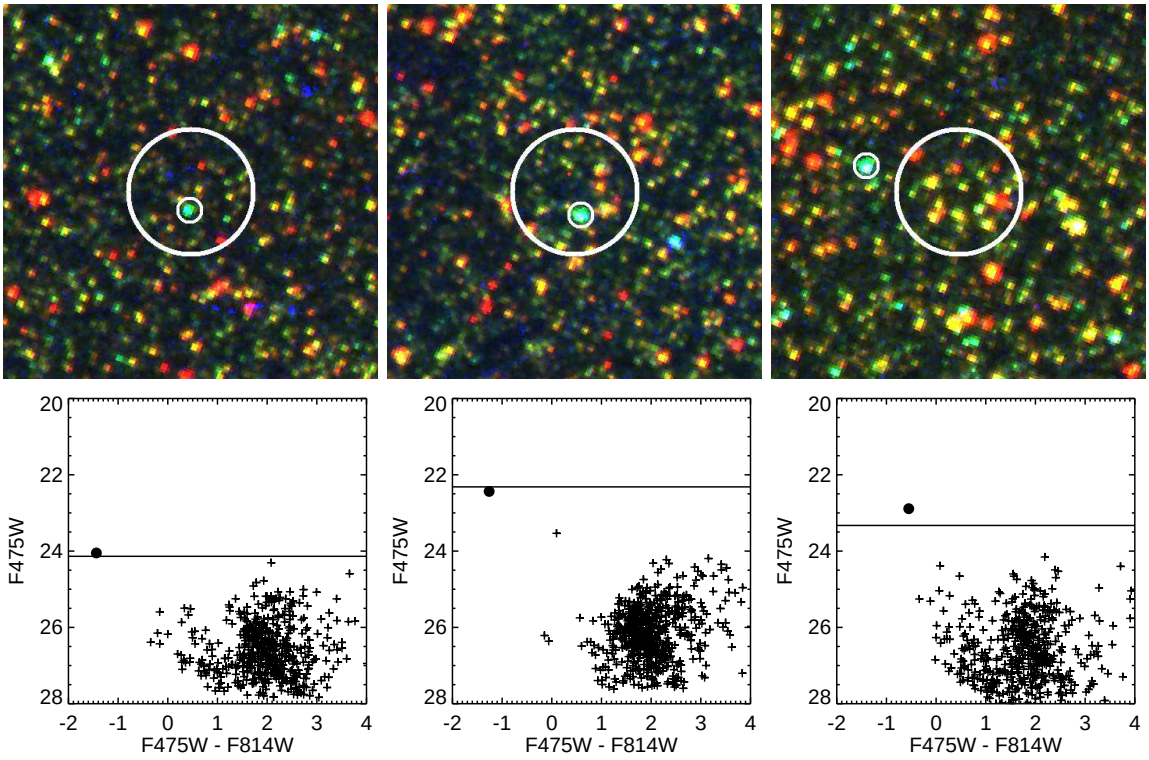

Fig. 2.— (Above) 3-color images of 3 PNe in PHAT. F814W, F475W, and F336W were used for the red, green, and blue images respectively so that PNe appear as bright, blue-green objects. PNe are marked by a small white circle. A larger white circle with a radius of 1″ is centered at the M06 RA and Dec for each PN. (Below) The respective optical CMD with a filled, black circle denoting the PN and pluses denoting stars within 3″ of the PN. A black line denotes the expected F475W magnitude estimated from the M06 $m5007$. From left to right the sources are M06 3015 (a typical PN), M06 938 (a bright, crowded PN), and M06 2665 (a bright, offset PN).

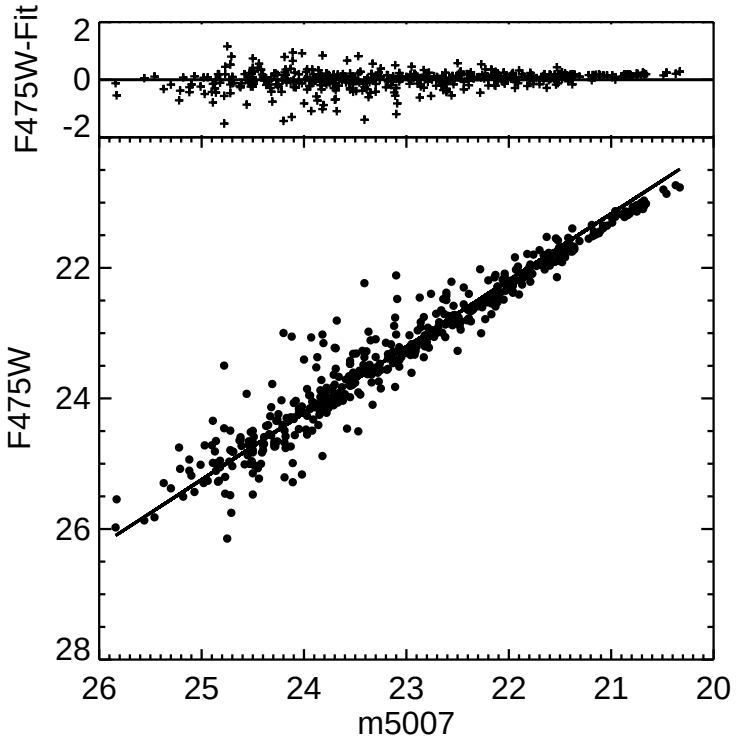

Fig. 3.— The linear relation between $m5007$ and F475W magnitudes of the final PHAT PNe catalog. This plot shows the strong dependence of F475W magnitude on [O III] λ5007 line strength. The linear fit was calculated taking into account the quoted M06 $m5007$ uncertainty as well as the PHAT Poisson errors from F475W photometry.

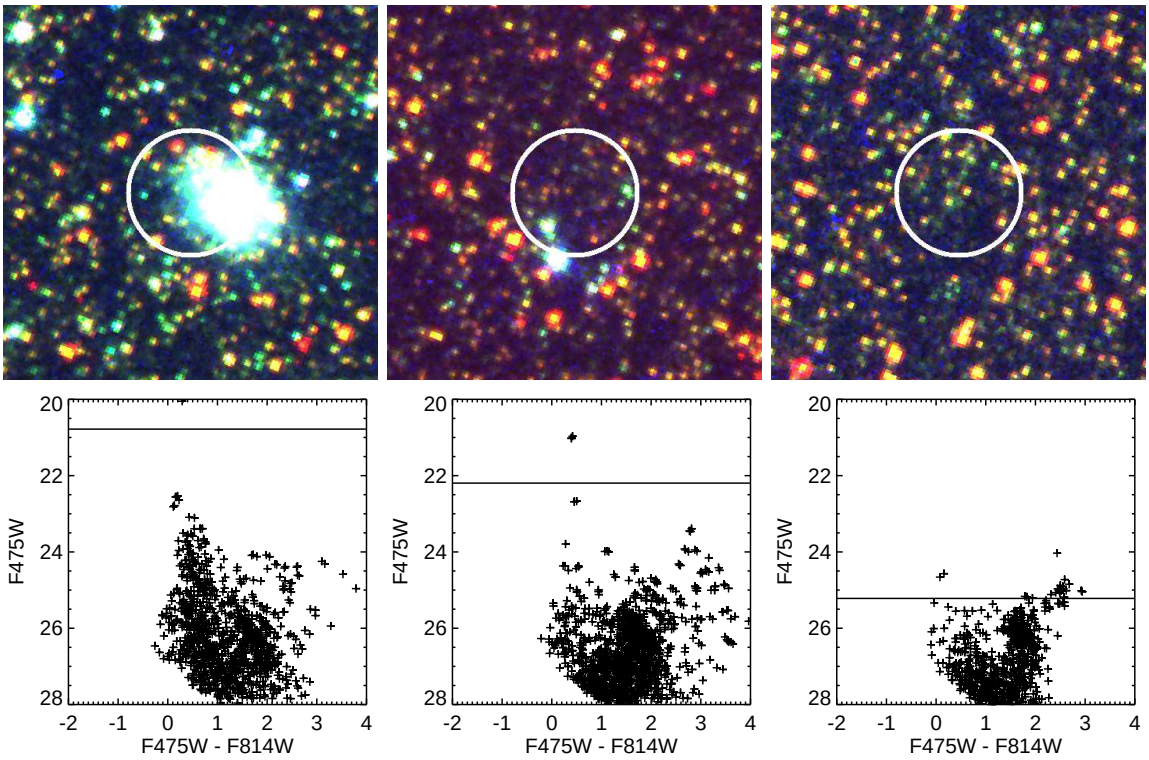

Fig. 4.— (Above) 3-color images of 3 M06 PN locations where no PN candidate could be determined in PHAT. A large white circle with a radius of 1″ is centered at the M06 RA and Dec for each PN. (Below) The respective optical CMD of stars within 3″ of the M06 PN location. A black line denotes the expected F475W magnitude estimated from the M06 $m5007$. From left to right the sources are M06 2721 (a large, bright H II region), M06 1378 (a possible Wolf Rayet star), and M06 731 (no PN candidate in PHAT).

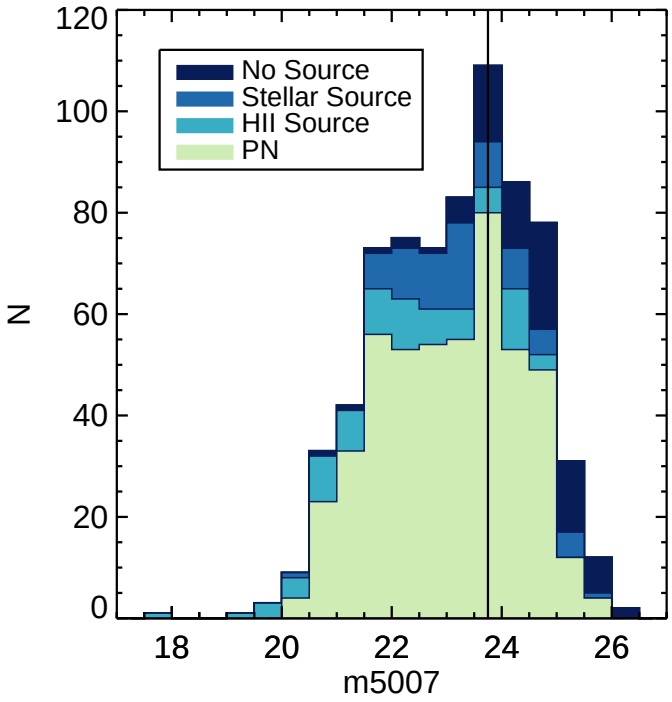

Fig. 5.— Histograms of visually identified sources for all 711 M06 PNe that fall under the PHAT footprint. The faint end is dominated by fields where no PN could be identified in PHAT and there were no obvious sources of possible misdetection. A black line is drawn at the reported M06 completeness limit of $m5007 = 23.75$.

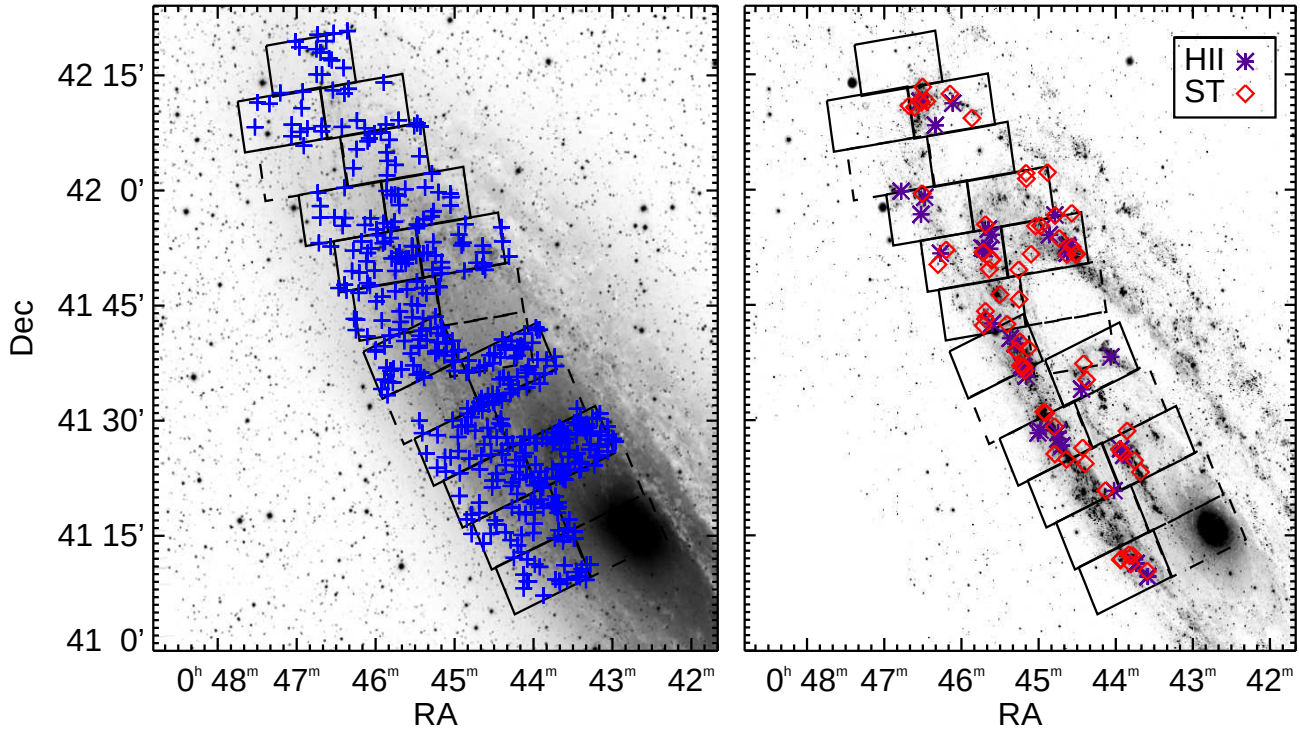

Fig. 6.— (Left) Blue crosses denote the location of matched PNe in the PHAT dataset over an optical image of M31 (credit and copyright: Martin Pugh `http://www.martinpughastrophotography.id.au/`). The PHAT bricks currently cross matched with M06 are outlined in solid black lines. The full PHAT footprint is outlined in dashed black lines. (Right) The location of non-PN sources (extended "HII" regions and non-PN "ST"ellar sources) over a GALEX UV image (Thilker et al. 2005). PN spatial density falls off radially while non-PN sources are clustered around UV bright regions. Non-PN objects were rejected without prior knowledge of their location.

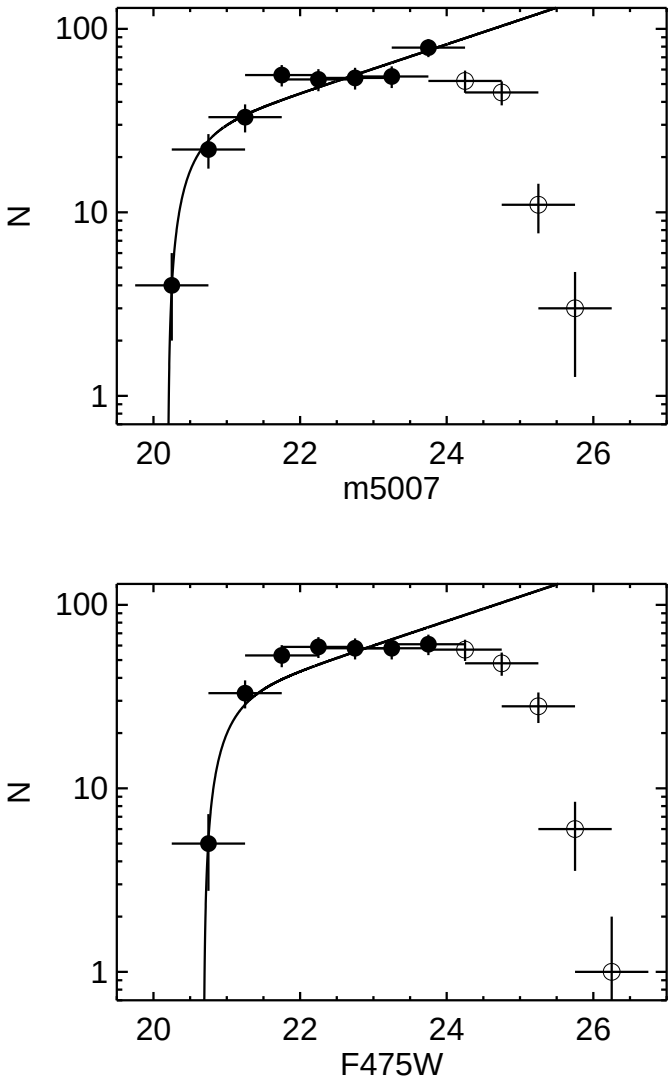

Fig. 7.— The PN luminosity function of the PHAT PNe catalog using $m5007$ (above) and F475W (below). The solid line shows the best fit to the PNLF as described by Equation 3. Filled circles denote values brighter than the completeness limit of 24th magnitude. Open circles denote values fainter then 24th magnitude which were not used in the fit.

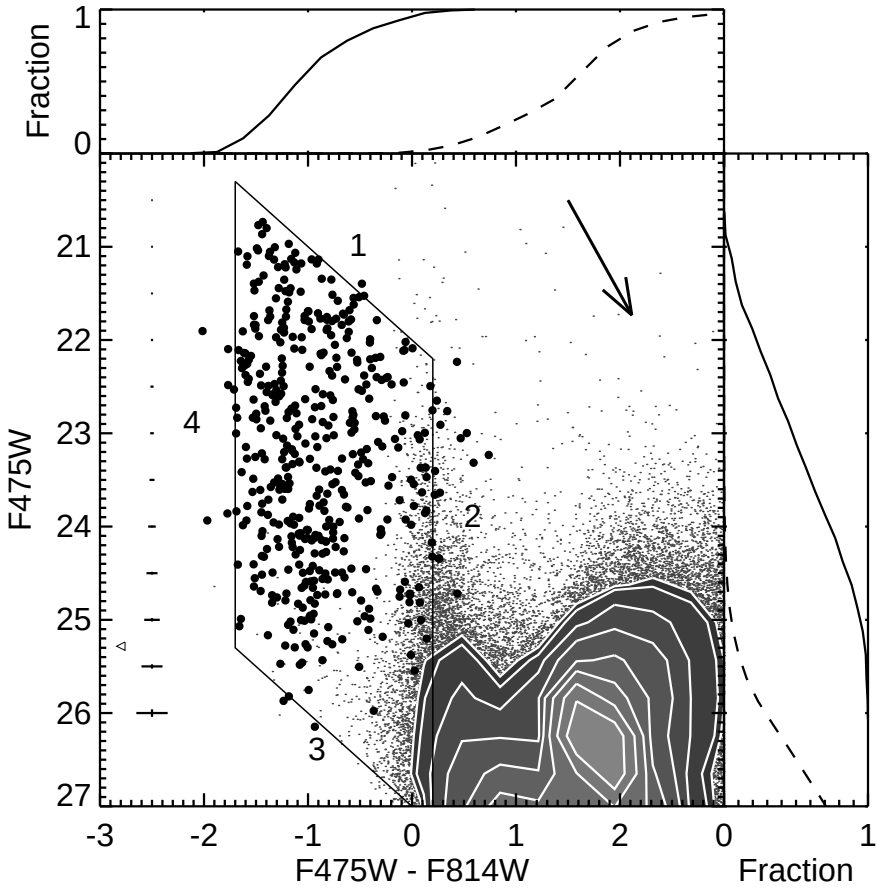

Fig. 8.— Black circles denote PNe. Background grey dots and contours indicate stars within 3″ of a PN. An open triangle at (-2.8, 25.3) represents the F475W magnitude of the one PN with F814W SNR < 4. A rhomboid with sides labeled 1, 2, 3, and 4 outlines the boundaries of the PNe population. Crosses along the left side of the plot indicate median Poisson errors from the photometry of PNe binned by F475W. A reddening vector shows the extinction effect of $A_V = 1$. (Above) The normalized cumulative distribution of F475W-F814W for PNe (solid line) and stars within 3″ of a PN (dashed line). (Right) The normalized cumulative distribution of F475W for PNe (solid line) and stars within 3″ of a PN (dashed line). PNe exist in a unique bright-blue region of PHAT optical CMDs.

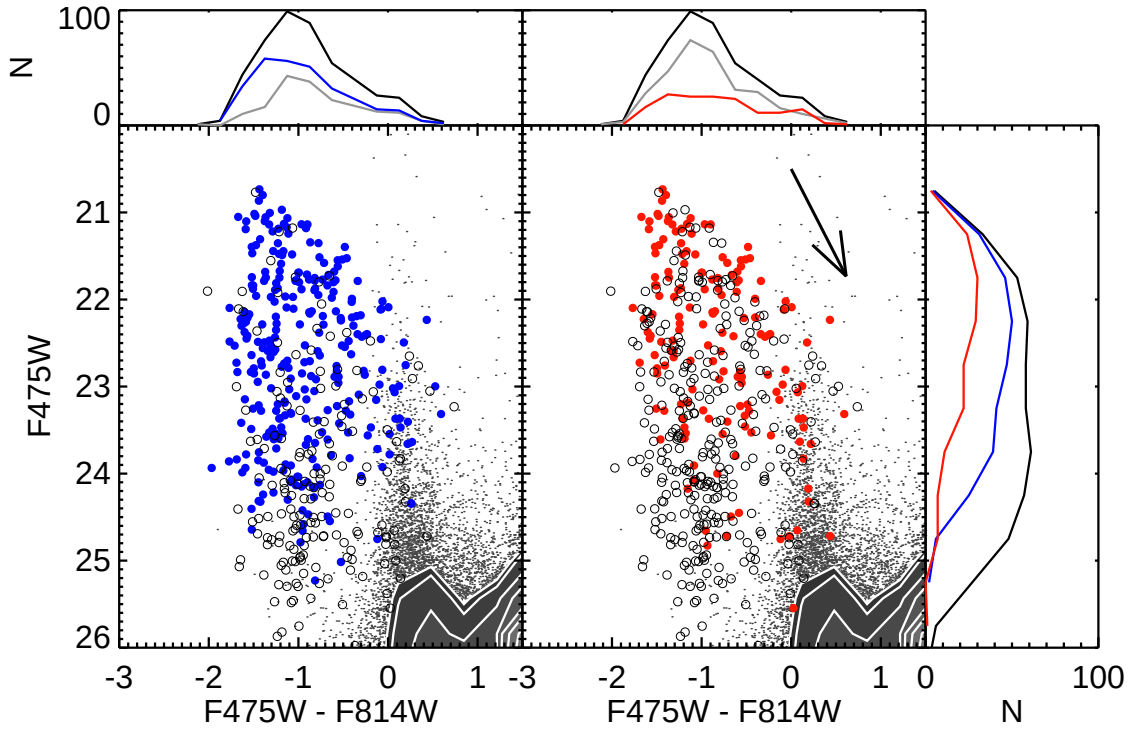

Fig. 9.— (Bottom, Left) Filled, blue circles denote PNe with detections in both UV filters. Open circles denote PNe without detections in both UV filters. Background grey dots and contours indicate all stars within 3″ of a PN. (Bottom, Center) Filled, red circles denote PNe with detections in both NIR filters. Open circles denote PNe without detections in both NIR filters. Background grey dots and contours indicate all stars within 3″ of a PN. A reddening vector shows the extinction effect of $A_V = 1$. (Top, Left) Distributions of F475W-F814W for all PNe (black line), PNe with UV detection (blue line), and PNe without UV detection (grey line). (Top, Right) Distributions of F475W-F814W for all PNe (black line), PNe with NIR detection (red line), and PNe without NIR detection (grey line). (Bottom, Right) Distributions of F475W for all PNe (black line), PNe with UV detection (blue line), and PNe with NIR detection (red line). UV and NIR detection is more common for PNe bright in F475W.

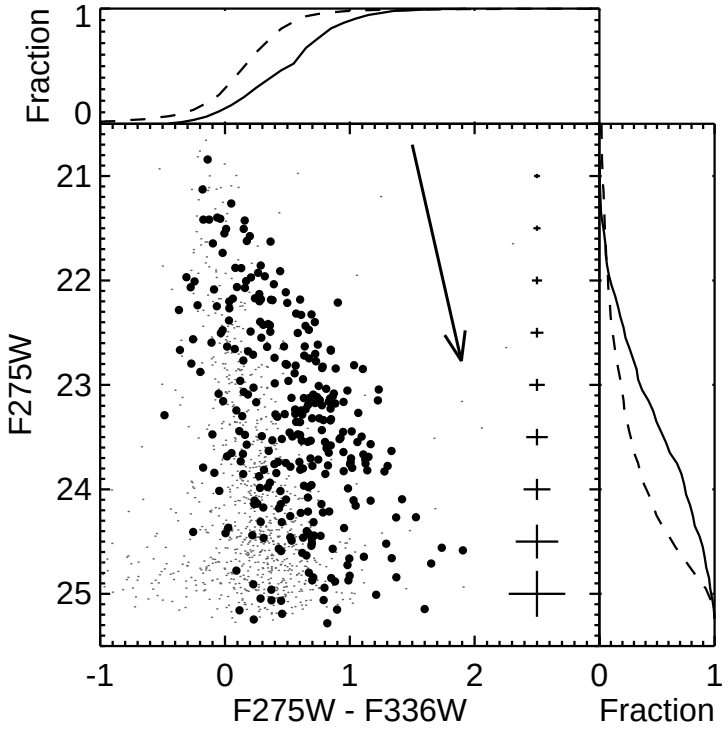

Fig. 10.— Filled, black circles denote PNe. Background grey dots indicate stars within 3″ of a PN. Crosses along the right side of the plot indicate median Poisson errors from the photometry of PNe binned by F275W. A reddening vector shows the extinction effect of $A_V = 1$. (Above) The normalized cumulative distribution of F275W-F336W for PNe (solid line) and stars within 3″ of a PN (dashed line). (Right) The normalized cumulative distribution of F275W for PNe (solid line) and stars within 3″ of a PN (dashed line). There are only slight differences between PNe and the population of hot MS stars in the PHAT UV CMD.

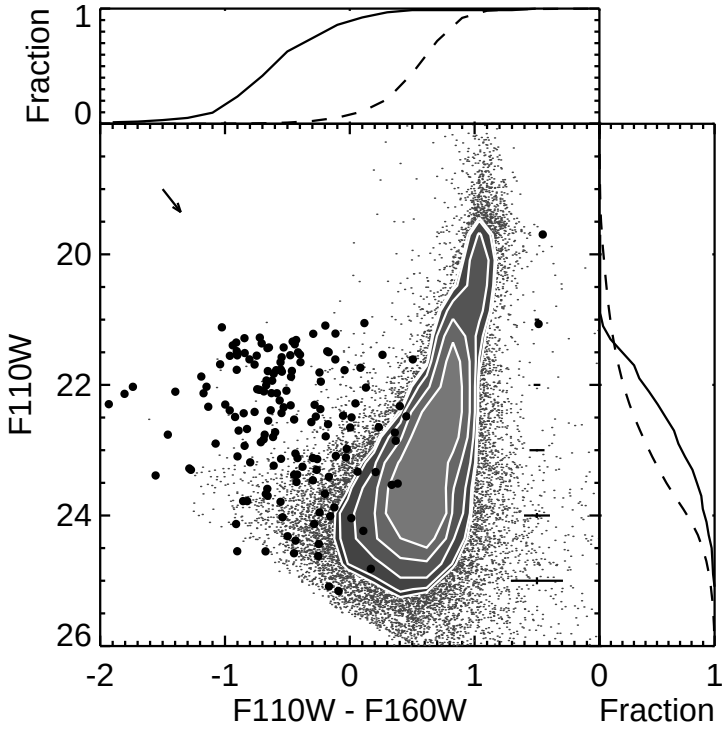

Fig. 11.— Filled, black circles denote PNe. Background grey dots and contours indicate stars within 3″ of a PN. Crosses along the right side of the plot indicate median Poisson errors from the photometry of PNe binned by F110W. A reddening vector shows the extinction effect of $A_V = 1$. (Above) The normalized cumulative distribution of F110W-F160W for PNe (solid line) and stars within 3″ of a PN (dashed line). (Right) The normalized cumulative distribution of F110W for PNe (solid line) and stars within 3″ of a PN (dashed line). PNe are bluer and brighter in the NIR than neighboring cool RGB and AGB stars.

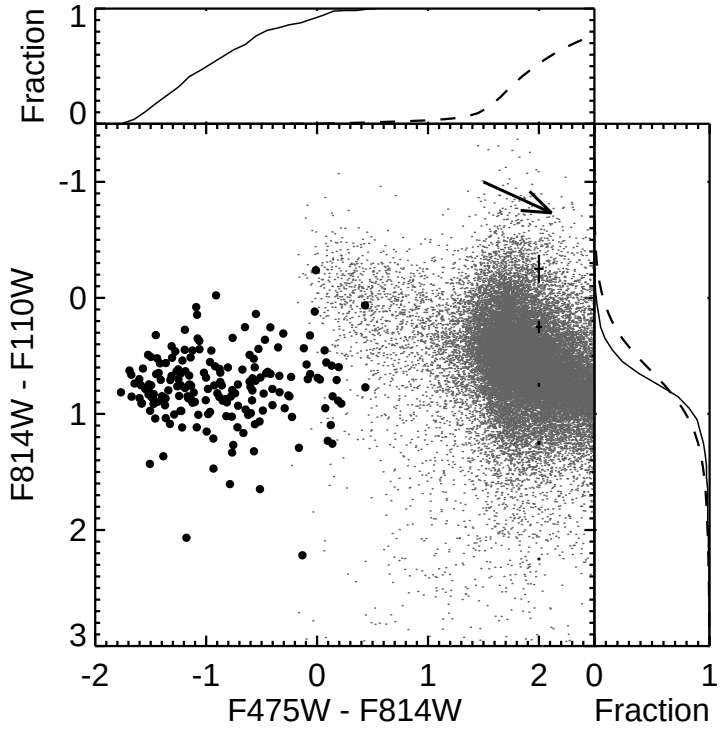

Fig. 12.— Filled, black circles denote PNe. Background grey dots indicate stars within 3″ of a PN. Crosses along the right side of the plot indicate median Poisson errors from the photometry of PNe binned by F814W-F110W. A reddening vector shows the extinction effect of $A_V = 1$. (Above) The normalized cumulative distribution of F475W-F814W for PNe (solid line) and stars within 3″ of a PN (dashed line). (Right) The normalized cumulative distribution of F814W-F110W for PNe (solid line) and stars within 3″ of a PN (dashed line). PNe are best distinguished from stars by their optical color.

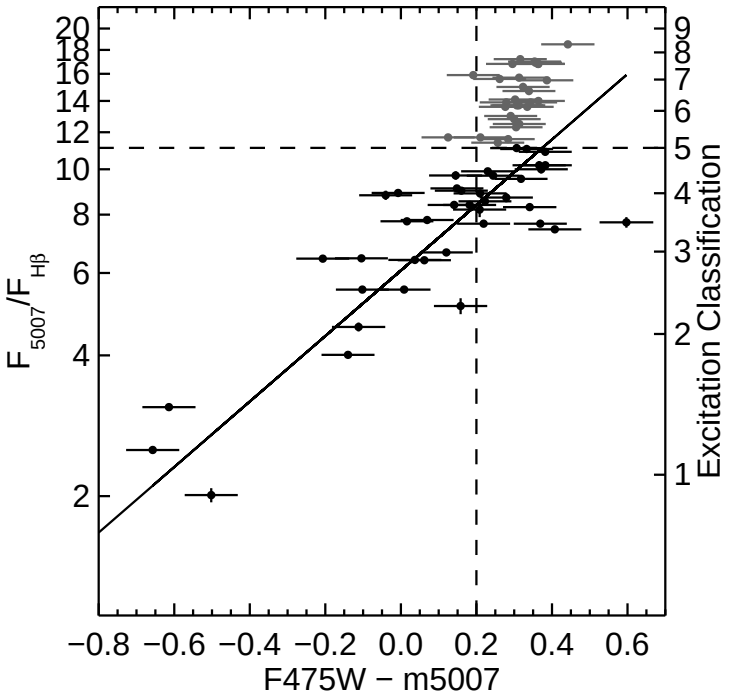

Fig. 13.— The relationship between the difference of F475W and $m5007$ magnitudes and the $F_{5007}/F_{H\beta}$ line ratio and Excitation classification ($EC \equiv 0.45(F_{5007}/F_{H\beta})$, for low EC PNe) using emission line flux ratios from Sanders et al. (2012). Black points denote low EC PNe ($EC < 5$), for which $H\beta$ makes a significant contributions to F475W flux. Grey points denote medium to high EC PNe ($EC > 5$), for which the EC cannot be accurately calculated from $F_{5007}/F_{H\beta}$. A solid line denotes a linear least squares fit between $F475W - m5007$ and $log\,(F_{5007}/F_{H\beta})$, ($RMSE = \pm 2.0$). The data has a correlation coefficient of 0.9. The largest source of error is the uncertainty in $m5007$ of 0.07 mag. Errors in $F_{5007}/F_{H\beta}$ are often smaller than the plot symbols. Dashed lines indicate where $F475W - m5007 = 0.2$ and where $EC = 5$. The majority of PNe with $F475W - m5007 < 0.2$ also have $EC < 5$.

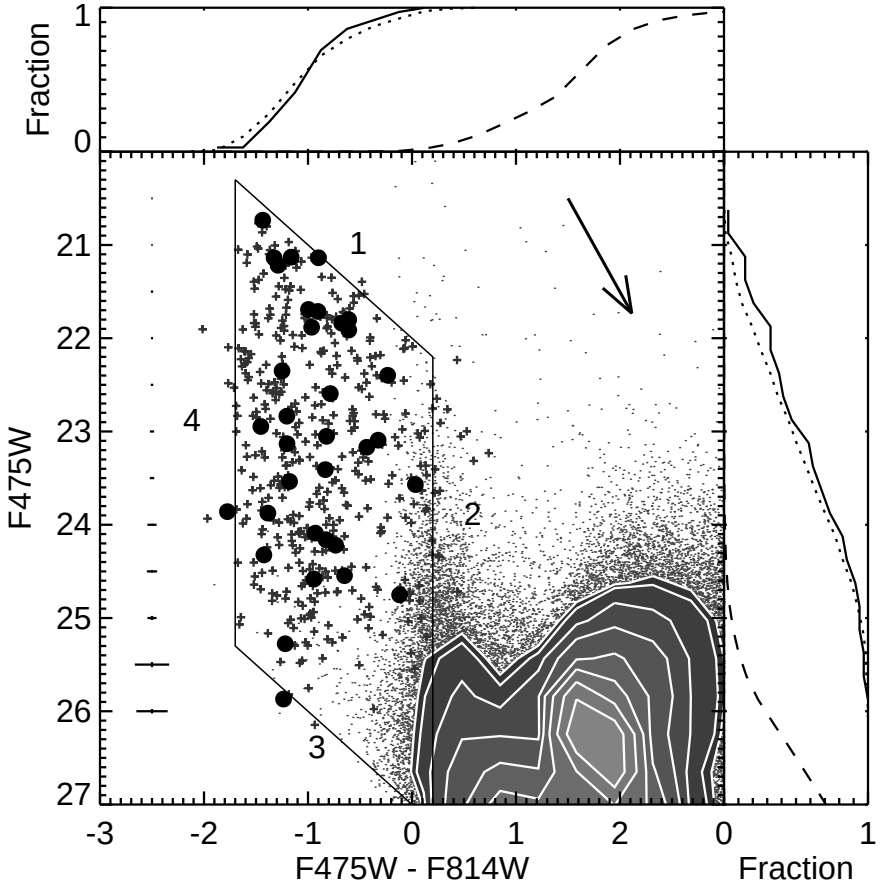

Fig. 14.— Same as Figure 8, but now large black circles and solid lines denote only PNe from "dust-free" regions. Grey crosses and dotted lines denote the full sample. The distribution is qualitatively very similar to that of the full sample suggesting the PHAT PNe catalog does not suffer large differential extinction.

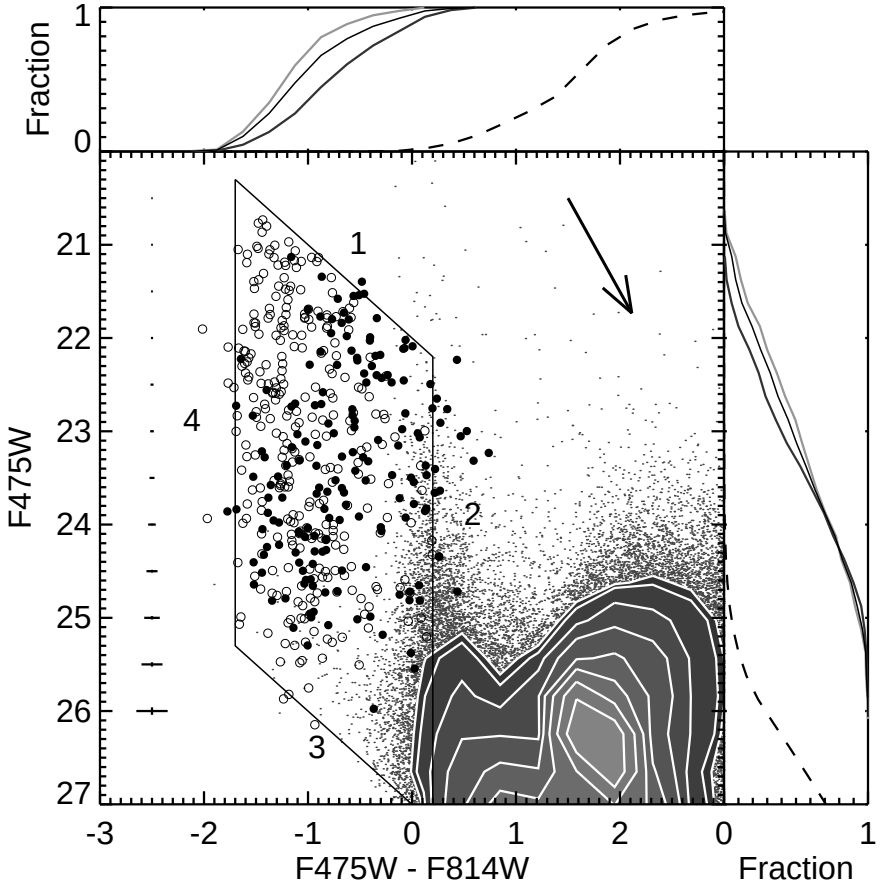

Fig. 15.— Filled, black circles denote low EC PNe. Open circles denote medium to high EC PNe. Background grey dots and contours indicate stars within 3″ of a PN. A rhomboid with sides labeled 1, 2, 3, and 4 outlines the boundaries of the PNe population. Crosses along the left side of the plot indicate median Poisson errors from the photometry of PNe binned by F475W. A reddening vector shows the extinction effect of $A_V = 1$. (Above) The normalized cumulative distribution of F475W-F814W for PNe (thin black line), low EC PNe (dark grey line), medium to high EC PNe (light grey line), and stars within 3″ of a PN (dashed line). (Right) The normalized cumulative distribution of F475W for PNe (thin black line), low EC PNe (dark grey line), medium to high EC PNe (light grey line), and stars within 3″ of a PN (dashed line). There is a distinct bright, blue population of medium to high EC PNe suggesting an evolutionary transition to higher F475W flux as increasing central star temperature increases excitation in the nebula.

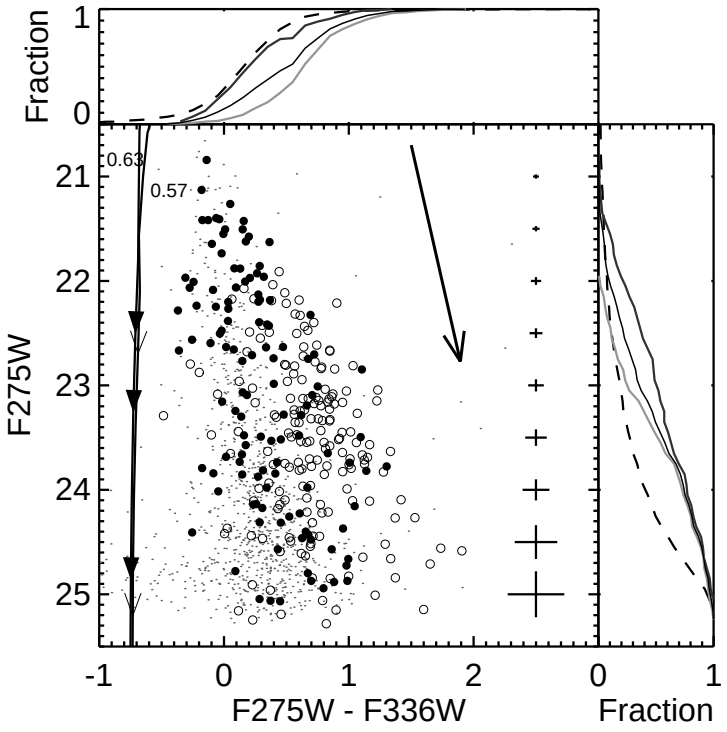

Fig. 16.— Filled, black circles denote low EC PNe. Open circles denote medium to high EC PNe. Background grey dots indicate stars within 3″ of a PN. Crosses along the left side of the plot indicate median Poisson errors from the photometry of PNe binned by F275W. A reddening vector shows the extinction effect of $A_V = 1$. Also shown are two unreddened P-AGB tracks for initial masses of $0.57M_\odot$ and $0.63M_\odot$. The tracks are nearly identical in this region of color-magnitude space. Open arrows indicate $0.57M_\odot$ 20,000 and 30,000 year ages. Filled arrows indicate $0.63M_\odot$ 2,000, 3,000, and 4,000 ages. (Above) The normalized cumulative distribution of F275W-F336W for PNe (thin black line), low EC PNe (dark grey line), medium to high EC PNe (light grey line), and stars within 3″ of a PN (dashed line). (Right) The normalized cumulative distribution of F275W for PNe (thin black line), low EC PNe (dark grey line), medium to high EC PNe (light grey line), and stars within 3″ of a PN (dashed line). Low EC PNe tend to be brighter and bluer than medium to high EC PNe in the PHAT UV CMD.

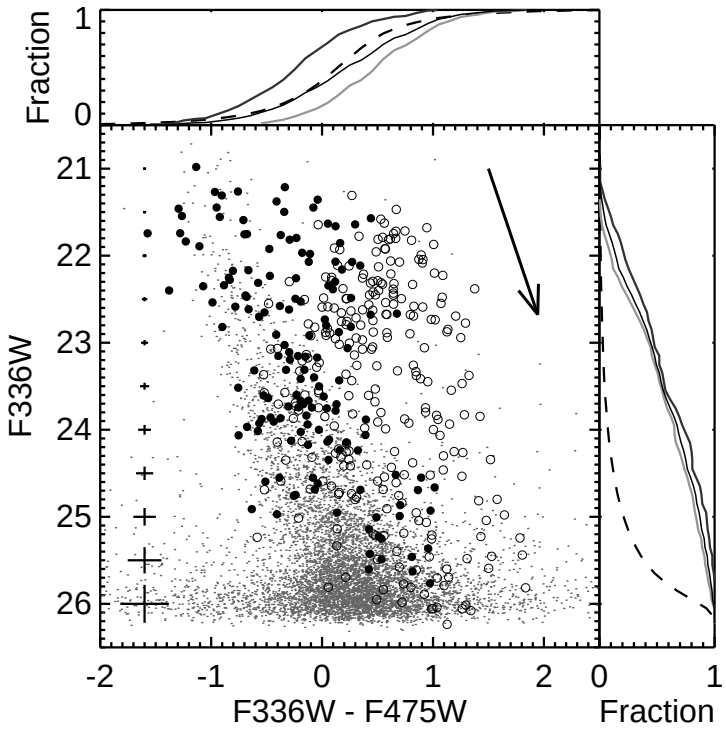

Fig. 17.— Filled, black circles denote low EC PNe. Open circles denote medium to high EC PNe. Background grey dots indicate stars within 3″ of a PN. Crosses along the left side of the plot indicate median Poisson errors from the photometry of PNe binned by F336W. A reddening vector shows the extinction effect of $A_V = 1$. (Above) The normalized cumulative distribution of F336W-F475W for PNe (thin black line), low EC PNe (dark grey line), medium to high EC PNe (light grey line), and stars within 3″ of a PN (dashed line). (Right) The normalized cumulative distribution of F336W for PNe (thin black line), low EC PNe (dark grey line), medium to high EC PNe (light grey line), and stars within 3″ of a PN (dashed line). A separation in excitation becomes apparent when comparing emission flux to continuum flux.

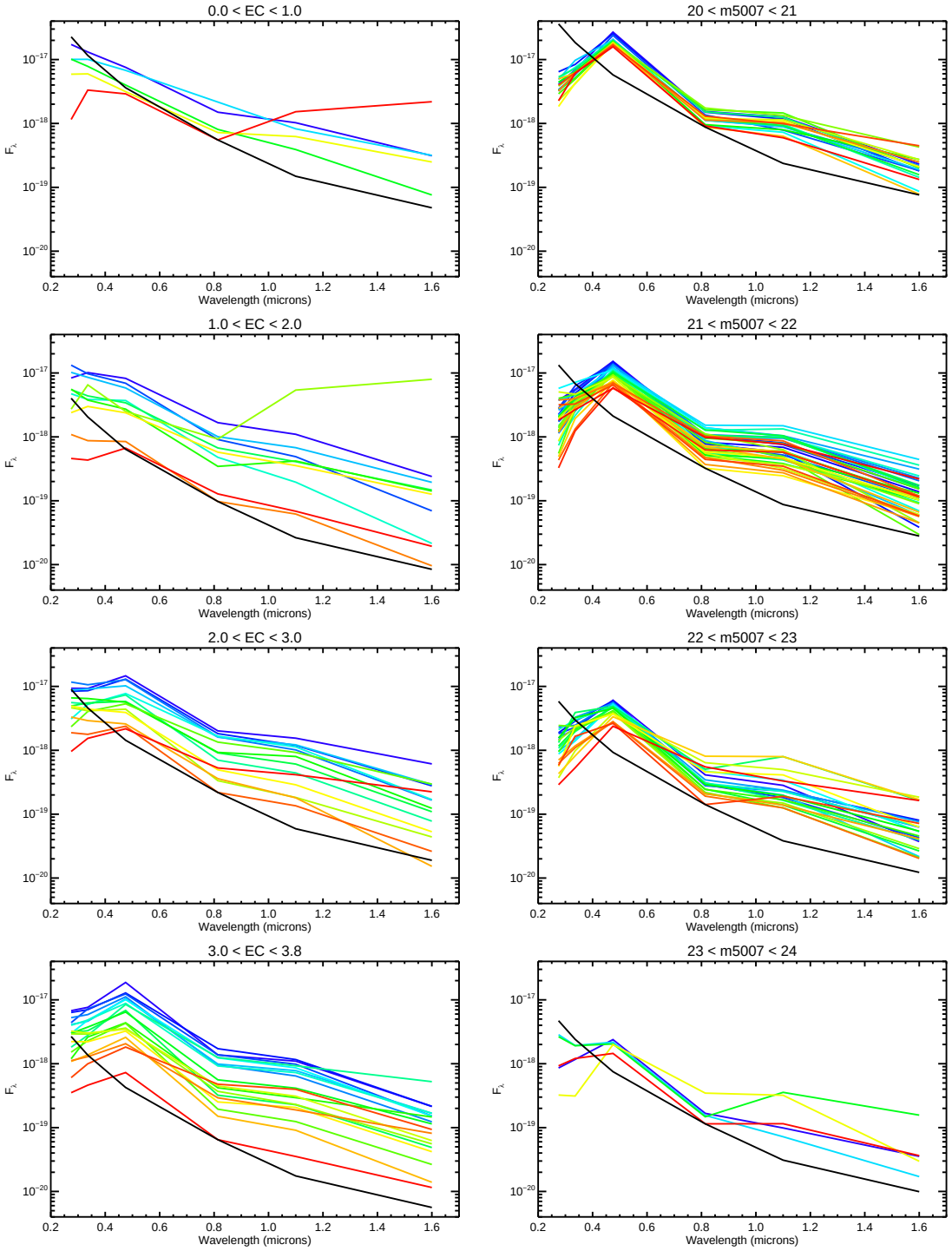

Fig. 18.— Spectral energy distributions of PHAT PNe with detections in all six bandpasses. The left column of plots shows SEDs of low EC PNe sorted by EC. The right column of plots show SEDs of medium to high EC PNe sorted by $m5007$. All SED plots are color-ranked by relative F475W flux. Black lines denote a 50,000 K black body curve accounting for full system throughput and extinction-corrected for $A_V = 0.17$ ($R_V = 3.1$), the average foreground extinction for the PHAT region (Schlafly & Finkbeiner 2011). Increasing excitation correlates to increasing emission line flux over the underlying continuum in the F475W and F110W bandpasses.

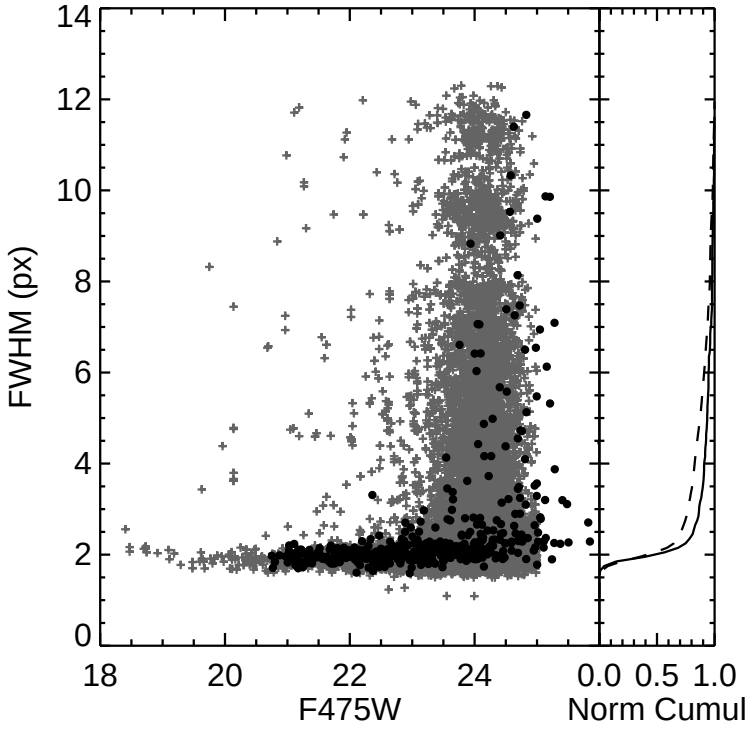

Fig. 19.— (Left) Direct FWHM measurements of PNe (black circles) and the 50 brightest stars with F475W<25 around each PN (grey pluses). FWHM values greater than ∼3 are likely due to poor direct FWHM measurement of faint, crowded sources. (Right) Normalized cumulative histograms of FWHM for PNe (solid line) and stars (dashed line). The PHAT PNe catalog does not appear extended compared to neighboring stars.

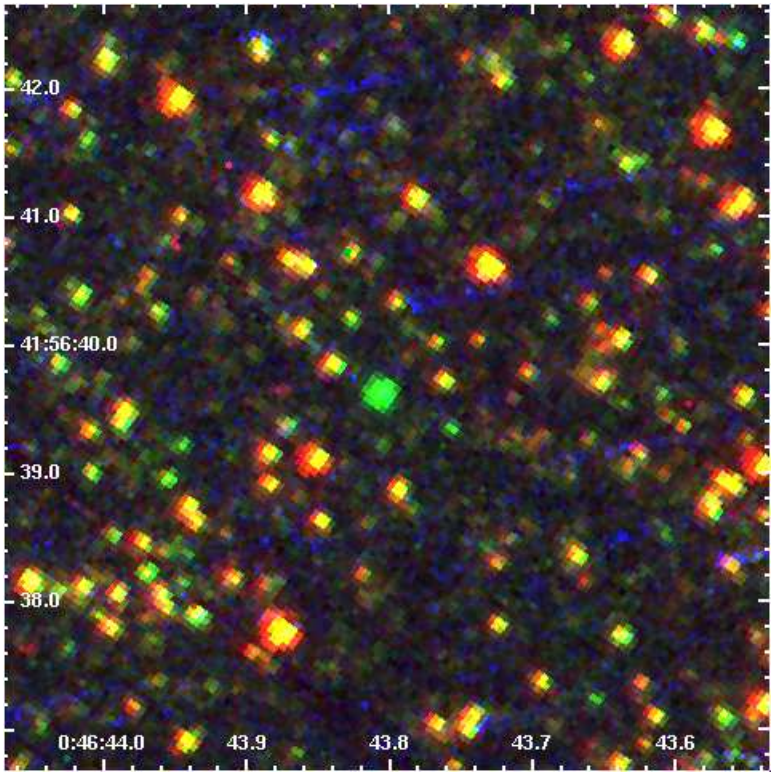

Fig. 20.— The bright, green object in the center of the frame is M06 143 - a slightly resolved PN candidate.

Table 1. Flux Contribution by Filter

Filter	Likely Main Flux Contributors
F275W	Stellar Continuum, Nebular Continuum, [Fe IV] λ2836, [Fe IV] λ2829, [Fe IV] λ2567, [C IV] λ2529, He II λ2733, He II λ2511, He II λ2386, [Ar IV] λ2854
F336W	Stellar Continuum, Nebular Continuum, Balmer Continuum, He II λ3203
F475W	He II λ4686, H I λ4861, H I λ4340, [Ar IV] λ4740, [O III] λ5007, [O III] λ4959
F814W	Stellar Continuum, Paschen Continuum, [Cr V] λ7979, He I λ7065, [S III] λ9069, [Ar III] λ7135
F110W	Stellar Continuum, He II λ10120, He I λ10830, H I λ12820, [S III] λ9532, [S III] λ9069
F160W	Stellar Continuum, He II λ4760

Note. — An extensive but incomplete list of likely flux contributors by filter.

Table 2. M31 PNe Photometric Catalog

M06 ID	PHAT RA	PHAT Dec	$F275W$	$F336W$	$F475W$	$F814W$	$F110W$	$F160W$	EC[a]	z_{PN}[b]
26	11.469719	42.086807	···	···	24.869	25.920	···	···	> 3.8	0.35
29	11.461526	42.113659	···	26.015	24.718	25.926	···	···	> 3.8	0.46
30	11.360975	42.142666	22.656	22.578	22.958	23.512	22.798	23.413	3.1	0.42
31	11.381368	42.144012	23.235	22.673	22.097	23.865	23.051	23.487	> 3.8	0.60
32	11.472247	42.147278	23.282	22.878	22.416	23.986	23.377	23.823	> 3.8	0.52
33	11.372000	42.149998	···	···	24.827	25.762	24.550	25.225	> 3.8	0.31
34	11.431614	42.156788	23.545	22.882	22.850	24.346	23.592	24.253	> 3.8	0.57
44	11.530962	42.110489	22.766	22.619	22.917	23.720	23.121	23.540	3.4	0.31
45	11.525844	42.116840	23.178	22.295	21.837	23.356	22.570	22.878	> 3.8	0.49
46	11.508853	42.127369	···	···	23.712	25.093	···	···	3.5	0.37
⋮	⋮	⋮	⋮	⋮	⋮	⋮	⋮	⋮	⋮	

Note. — Table 2 is published in its entirety in the electronic edition of the Astrophysical Journal. A portion is shown here for guidance regarding its form and content.

[a]Excitation Classification ($EC \equiv 0.45 \times (F_{5007}/F_{H\beta})$, for $EC < 5$) as estimated by $\log(F_{5007}/F_{H\beta}) = 0.7835 + 0.7003\,(F475W - m5007)$.

[b]The standard score of the deviation from typical PNe identified in PHAT. See Section 2.2.2 for full derivation.

Table 3. Misidentified Extended H II Regions

M06 ID	M06 RA	M06 Dec	M06 $m5007$	M06 ID	M06 RA	M06 Dec	M06 $m5007$
35	11.471667	42.159944	23.90	52	11.660417	42.182833	22.93
53	11.679167	42.185806	21.31	54	11.543750	42.189306	24.33
55	11.638333	42.193917	20.60	56	11.535000	42.192000	21.03
57	11.642917	42.195306	17.75	58	11.674167	42.196722	24.10
59	11.672917	42.199167	22.39	60	11.544167	42.212194	20.97
62	11.680417	42.218917	24.26	64	11.645417	42.195833	22.08
84	11.142083	41.954194	23.41	96	11.211250	41.936028	24.84
103	11.318750	41.958861	24.43	106	11.393750	41.969889	23.70
109	11.366667	41.991667	24.30	117	11.291667	42.028944	22.73
120	11.292917	42.041056	21.21	121	11.222500	42.042806	20.83
125	11.197500	41.950194	22.46	126	11.197083	41.949361	20.92
139	11.435833	41.957500	21.99	147	11.637917	41.950833	23.49
150	11.640417	41.986750	24.02	163	11.625833	41.987694	22.78
241	11.129583	41.852500	23.86	242	11.124167	41.862889	24.08
243	11.158333	41.864722	22.23	246	11.125417	41.866167	22.65
257	11.183750	41.899778	21.29	262	11.247917	41.920083	24.35
268	11.191667	41.883028	23.50	279	11.413333	41.832139	23.39
285	11.405000	41.851889	21.10	295	11.434167	41.868667	21.20
298	11.428750	41.876278	21.67	301	11.430417	41.883417	19.67
307	11.406667	41.906722	22.84	322	11.581667	41.841889	22.11
324	11.573333	41.866194	19.19	327	11.555000	41.873556	21.66
446	11.285000	41.660750	22.30	448	11.327083	41.670500	21.64
481	11.298333	41.621306	22.08	482	11.327500	41.677833	24.12
494	11.431667	41.709944	22.32	659	11.252500	41.476778	20.03
660	11.253333	41.478361	21.43	661	11.187083	41.478083	22.74
739	11.291250	41.599917	21.51	741	11.308333	41.603917	21.42
954	10.913333	41.448028	20.35	996	10.979167	41.434611	21.93
999	11.160000	41.419861	20.89	1000	10.982917	41.442750	21.66
1020	11.197500	41.431500	21.90	1371	10.932917	41.193583	23.21
1377	10.945417	41.211056	22.46	1385	11.062917	41.258722	23.57
1699	10.895000	41.164944	19.97	2159	11.675000	42.262694	24.80
2581	11.564583	42.249167	24.53	2587	11.148333	41.935139	23.22
2589	11.416250	41.919278	23.11	2664	11.103750	41.627583	22.88
2669	11.296250	41.612583	22.18	2673	11.301667	41.619278	20.52
2674	11.299167	41.620250	20.06	2675	11.302500	41.621250	20.82
2678	11.309583	41.623639	21.73	2720	11.203333	41.453583	24.37
2721	11.187500	41.464028	20.60	2722	11.181250	41.465694	24.10
2994	11.244583	41.927028	20.15	3091	11.212917	41.923278	24.28
3158	10.895417	41.164583	19.86	3225	11.302083	41.621583	20.78

Note. — M06 sources that are visually extended in PHAT images and excluded from the PHAT PNe catalog. Most are likely H II regions.

Table 4. Misidentified Stellar Sources

M06 ID	PHAT RA	PHAT Dec	$F275W$	$F336W$	$F475W$	$F814W$	$F110W$	$F160W$
65	11.592355	42.143700	19.167	19.380	20.748	20.610	20.683	20.566
66	11.620730	42.196083	19.415	19.446	20.632	20.228	20.124	20.020
100	...	...	...	...	...	...	...	...
105	11.379783	41.964077	23.464	22.513	21.697	20.973	20.722	20.429
111	11.204804	41.991951	22.436	22.297	23.064	22.518	...	...
116	11.384217	42.012291	24.817	22.829	21.228	19.848	19.489	19.003
127	11.369970	41.954872	20.679	20.608	21.725	21.205	21.113	20.974
151	...	...	...	...	...	...	...	...
152	11.703743	42.000370	21.215	21.010	21.024	19.468	...	...
153	11.630049	42.009483	22.363	21.906	22.805	22.122	...	...
⋮	⋮	⋮	⋮	⋮	⋮	⋮	⋮	⋮

Note. — M06 sources that are likely misidentified non-PN stellar sources and excluded from the PHAT PNe catalog. PHAT RA, Dec, and photometry is included when available. Table 4 is published in its entirety in the electronic edition of the Astrophysical Journal. A portion is shown here for guidance regarding its form and content.